

mLaSDI: Multi-stage latent space dynamics identification

William Anderson^{a,*}, Seung Whan Chung^a, Robert Stephany^a, Youngsoo Choi^a

^a*Lawrence Livermore National Laboratory, Livermore, CA 94550, United States*

Abstract

Accurately solving partial differential equations (PDEs) is essential across many scientific disciplines. However, high-fidelity solvers can be computationally prohibitive, motivating the development of reduced-order models (ROMs). Recently, Latent Space Dynamics Identification (LaSDI) was proposed as a data-driven, non-intrusive ROM framework. LaSDI compresses the training data via an autoencoder and learns user-specified ordinary differential equations (ODEs), governing the latent dynamics, enabling rapid predictions for unseen parameters. While LaSDI has produced effective ROMs for numerous problems, the autoencoder must simultaneously reconstruct the training data and satisfy the imposed latent dynamics, which are often competing objectives that limit accuracy, particularly for complex or high-frequency phenomena. To address this limitation, we propose multi-stage Latent Space Dynamics Identification (mLaSDI). With mLaSDI, we train LaSDI sequentially in stages. After training the initial autoencoder, we train additional decoders which map the latent trajectories to residuals from previous stages. This staged residual learning, combined with periodic activation functions, enables recovery of high-frequency content without sacrificing interpretability of the latent dynamics. Numerical experiments on a multiscale oscillating system, unsteady wake flow, and the 1D-1V Vlasov equation demonstrate that mLaSDI achieves significantly lower reconstruction and prediction errors, often by an order of magnitude, while requiring less training time and reduced hyperparameter tuning compared to standard LaSDI.

Keywords:

*Corresponding Author: anderson316@llnl.gov

1. Introduction

Advances in computational power and numerical techniques have enabled increasingly accurate and complex simulations of time-dependent partial differential equations (PDEs). High-fidelity numerical simulations improve understanding in many scientific fields such as engineering [10, 19, 33], physics [48, 50] and biology [39]. While accurate, these simulations are often computationally prohibitive, which necessitates the use of reduced-order models (ROMs). In this work, we focus on parametric PDEs, where input parameters influence the initial conditions or underlying physics.

There exists rich theory for projection-based ROMs, where the governing equations are known [3, 5]. However, linear projection-based approaches such as the proper orthogonal decomposition struggle with advection-dominated problems [41, 45]. Nonlinear projection techniques have shown improved accuracy for these problems [7, 20, 34, 14, 12, 37, 17, 13, 35, 15], but remain intrusive, require knowledge of the governing equations.

Another approach is to use non-intrusive reduced-order models, which are purely data-driven. These approaches develop ROMs without any knowledge of the underlying PDE. Yet, many non-intrusive approaches lack interpretability, which makes it difficult to generalize results beyond the training regime. This is the main motivation for the reduced-order modeling framework introduced by Fries et al. [21], Latent Space Dynamics Identification (LaSDI). LaSDI trains an autoencoder and learns interpretable dynamics of the compressed data by applying Sparse Identification of Nonlinear Dynamics (SINDy) [9] in the latent space. By interpolating the learned ODE coefficients, LaSDI enables rapid predictions for unseen parameter values. Since its inception, there have been several improvements and variations to the LaSDI algorithm [6, 24, 25, 40, 49, 27, 16, 26, 8]. For example, developments include simultaneous training of the autoencoder and SINDy with residual-based active learning [24], the introduction of Gaussian Processes (GPs) to interpolate for SINDy coefficients [6], implementations of weak-form SINDy to deal with noisy data [25, 49], and implementing physical constraints in the latent space [40, 27].

Despite these advances, a fundamental tension remains: the autoencoder must simultaneously reconstruct training data accurately and produce latent

trajectories that satisfy the prescribed ODE structure. These competing objectives often compromise both reconstruction quality and predictive accuracy, particularly for complex or high-frequency dynamics. There is a well-known spectral bias of neural networks toward low frequencies [44, 52, 53], which is exacerbated by imposing smooth latent dynamics on our autoencoder. In practice, achieving acceptable performance with LaSDI may require large autoencoders and extensive hyperparameter tuning.

To overcome these limitations, we introduce **multistage Latent Space Dynamics Identification (mLaSDI)**, a framework that extends any variant of LaSDI by training multiple networks sequentially. After the initial autoencoder is trained, subsequent stages introduce new decoders which map the same latent trajectories to the residuals from previous stages. Because all stages share a common latent representation, we preserve interpretability of the latent dynamics while dramatically improving reconstruction accuracy. We will show that for some examples, mLaSDI improves reconstruction accuracy by an order of magnitude with reduced training time and less hyperparameter sensitivity. Source code for this project is based on GPLaSDI: <https://github.com/LLNL/GPLaSDI>.

1.1. Related Works

Several works have applied equation-learning algorithms [9, 46] to approximate the underlying latent space dynamics [4, 18, 31, 43]. Perhaps the most closely related work to LaSDI is that of Champion et al. [11], who train an autoencoder to learn a SINDy representation in the latent space. However, their method is not parameterized and therefore less generalizable than LaSDI.

Multiple authors have also proposed the idea of training sequential neural networks in other contexts to achieve increased accuracy. Both [1] and [52] introduce multi-stage neural networks, where each stage a new network is introduced to learn the error from the previous stages. In [52] the initial weights of the networks are altered in order to learn the residual more quickly, while [1] increases the network size at each stage. For physics-informed neural networks, [29] proposes a stacked architecture combining linear and nonlinear networks at each stage. Several authors [51, 54, 55] have also explored the use of stacked autoencoders to increase reconstruction accuracy.

While multi-stage architectures exist in other contexts, none of these methods address the interpretability–accuracy trade-off inherent to LaSDI and other models with an interpretable latent space. To our knowledge, mLaSDI

is the first multi-stage architecture designed for interpretable latent dynamics, where each stage must respect dynamical constraints. This is a notable departure from previous residual-learning networks and a fundamentally different challenge compared to prior stacked architectures.

We emphasize that the goal of this manuscript is not to provide comparison with other popular residual-based learning approaches, but instead to provide a framework that can fundamentally improve results for many of the different LaSDI approaches. We demonstrate the performance of mLaSDI on several benchmark problems, showing that mLaSDI outperforms traditional LaSDI variants both in accuracy and computational efficiency.

1.2. Outline

In section 2 we describe our problem setting and the LaSDI algorithm. In section 3 we describe the mLaSDI algorithm. In section 4 we provide numerical examples, and in section 5 we provide our concluding remarks.

2. LaSDI Framework

Before discussing mLaSDI, we must briefly describe the LaSDI algorithm. Most variations to the LaSDI algorithm differ only in their choice of dynamics identification in the latent space, or the choice of interpolation scheme for learned dynamics. In either case, the mLaSDI framework we introduce in Section 3 applies broadly to all such variants.

2.1. Governing Equations

We consider parameterized ODEs of the form

$$\frac{d}{dt}\mathbf{u}(t; \boldsymbol{\mu}) = \mathbf{f}(\mathbf{u}; \boldsymbol{\mu}), \quad \mathbf{u}(0; \boldsymbol{\mu}) = \mathbf{u}_0(\boldsymbol{\mu}), \quad (1)$$

where $\mathbf{u} : \mathbb{R}^+ \rightarrow \mathbb{R}^{N_u}$ is the state vector, $\mathbf{f} : \mathbb{R}^{N_u} \rightarrow \mathbb{R}^{N_u}$ is a (possibly nonlinear) vector-valued function, and $\boldsymbol{\mu} \in \mathcal{D} \subset \mathbb{R}^N$ is an input parameter. This parameter may affect either the physics of the simulation or the initial condition. Our dynamical system (1) often arises from the spatial discretization of a PDE, although this need not be the case. The goal of LaSDI is to rapidly predict the evolution of the state vector \mathbf{u} for unseen input parameter values.

We assume no knowledge of the function \mathbf{f} , and only consider snapshots of the state vector at discrete times \mathbf{u} at times t_i , $i = 0, 1, \dots, N_t$. For simplicity,

we assume uniform timestep size $\Delta t = t_{i+1} - t_i$. For a given an input parameter $\boldsymbol{\mu}^{(i)}$, we form snapshots of the state vector into the training data matrix $U^{(i)} = [\mathbf{u}^{(i)}(0), \mathbf{u}^{(i)}(t_1), \dots, \mathbf{u}^{(i)}(t_{N_t})] \in \mathbb{R}^{(N_u \times (N_t+1))}$. Concatenating the snapshots from each of our N_μ training parameters yields the tensor

$$\mathbf{U} = [U^{(1)}, U^{(2)}, \dots, U^{(N_\mu)}] \in \mathbb{R}^{N_\mu \times (N_t+1) \times N_u}, \quad (2)$$

where \mathbf{U} is our training data tensor.

2.2. Data compression

Often the state dimension N_u is large, and so we compress the data to facilitate easier analysis and modeling. In this manuscript, we always compress the training data \mathbf{U} with an autoencoder [28], as this generally allows for smaller latent dimension and higher reconstruction accuracy than linear methods.

These autoencoders consist of an encoder map which compresses the data, and a decoder map which attempts to project the compressed data back to the original state. More precisely, the encoder learns a map $\mathcal{G}_{\text{enc}} : \mathbb{R}^{N_u} \rightarrow \mathbb{R}^{N_z}$ and the decoder learns the map $\mathcal{G}_{\text{dec}} : \mathbb{R}^{N_z} \rightarrow \mathbb{R}^{N_u}$, where $N_z \ll N_u$. Applying the encoder to each snapshot gives the latent representation

$$\mathbf{z}^{(i)}(t_k) := \mathcal{G}_{\text{enc}}(\mathbf{u}^{(i)}(t_k)) \in \mathbb{R}^{N_z}. \quad (3)$$

We can similarly map the training data matrix $U^{(i)}$ to a low dimensional compressed training to obtain a compressed training data matrix and tensor given by

$$Z^{(i)} = [\mathbf{z}^{(i)}(t_0), \mathbf{z}^{(i)}(t_1), \dots, \mathbf{z}^{(i)}(t_{N_t})], \quad (4)$$

$$\mathbf{Z} = [Z^{(1)}, Z^{(2)}, \dots, Z^{(N_\mu)}] \in \mathbb{R}^{N_\mu \times (N_t+1) \times N_z}. \quad (5)$$

We also define the autoencoder reconstruction of our training data tensor $\hat{\mathbf{U}}$, given by

$$\hat{\mathbf{U}} := \mathcal{G}_{\text{dec}} \mathcal{G}_{\text{enc}} \mathbf{U}. \quad (6)$$

Our autoencoder then attempts to minimize the reconstruction loss

$$\mathcal{L}_{\text{AE}}(\boldsymbol{\theta}_{\text{enc}}, \boldsymbol{\theta}_{\text{dec}}) = \|\mathbf{U} - \hat{\mathbf{U}}\|^2, \quad (7)$$

where $\|\cdot\|$ is the element-wise ℓ^2 -norm.

2.3. Latent Space Dynamics Identification

Autoencoders allow us to compress the training data, but they do not provide any interpretability in the latent space. To address this, LaSDI imposes user-specified dynamics in the latent space which the autoencoder attempts to satisfy.

Applying SINDy [9], we approximate the time derivative of our compressed snapshots with a library of functions satisfying

$$\dot{Z}^{(i)} \approx \hat{Z}^{(i)} := \Theta(Z^{(i)})\Xi^{(i)}, \quad (8)$$

where $\Theta(Z^{(i)})$ is a user-chosen library of functions and $\Xi^{(i)}$ is a coefficient matrix to be determined. While we are free to choose any terms in our library, a common choice for LaSDI variants is to assume linear dynamics [6, 24] so that the library and coefficients are given by

$$\Theta(Z^{(i)}) = (\mathbf{1} \ (Z^{(i)})^\top), \quad \Xi^{(i)} = (\mathbf{b}^{(i)} \ A^{(i)})^\top, \quad (9)$$

where $\mathbf{1} \in \mathbb{R}^{N_t}$ is a vector with all entries equal to 1, and we must solve for the coefficients $\mathbf{b}^{(i)} \in \mathbb{R}^{N_z}$ and $A^{(i)} \in \mathbb{R}^{N_z \times N_z}$. We will also assume linear dynamics for all LaSDI examples described in this paper. This choice is due to both simplicity and stability, discussed further in [Appendix B](#).

To determine the coefficients $\Xi^{(i)}$, we solve the least squares problem

$$\min_{\mathbf{b}^{(i)} \in \mathbb{R}^{N_z}, A^{(i)} \in \mathbb{R}^{N_z \times N_z}} \|\hat{Z}^{(i)} - (\mathbf{1} \ (Z^{(i)})^\top)(\mathbf{b}^{(i)} \ A^{(i)})^\top\|^2. \quad (10)$$

While many applications of SINDy enforce sparsity in the coefficient matrix (as the algorithm’s name implies), we use a dense coefficient matrix. This allows us to retain greater representation power in the latent space. Additionally, if we enforced sparsity, the SINDy coefficients corresponding to each training parameter would yield a different sparsity pattern. This sparsity would then be violated with the interpolation scheme described in [Section 2.4](#)

After solving the least squares problem (10) for each of our N_μ simulations, we form tensors for our SINDy approximations of the latent space dynamics and the corresponding coefficient matrices

$$\hat{\mathbf{Z}} = [\hat{Z}^{(1)} \ \hat{Z}^{(2)} \ \dots \ \hat{Z}^{(N_\mu)}] \in \mathbb{R}^{N_\mu \times (N_t+1) \times N_z} \quad (11)$$

$$\Xi = [\Xi^{(1)} \ \Xi^{(2)} \ \dots \ \Xi^{(N_\mu)}] \in \mathbb{R}^{N_\mu \times N_z \times (N_z+1)}. \quad (12)$$

We can now define our dynamics identification loss

$$\mathcal{L}_{\text{DI}}(\Xi) = \|\dot{\mathbf{Z}} - \hat{\dot{\mathbf{Z}}}\|^2. \quad (13)$$

Additionally, we penalize the norm of our SINDy coefficients to obtain the loss function for LaSDI

$$\mathcal{L}(\boldsymbol{\theta}_{\text{enc}}, \boldsymbol{\theta}_{\text{dec}}, \Xi) = \mathcal{L}_{\text{AE}}(\boldsymbol{\theta}_{\text{enc}}, \boldsymbol{\theta}_{\text{dec}}) + \beta_1 \mathcal{L}_{\text{DI}}(\Xi) + \beta_2 \|\Xi\|^2 \quad (14)$$

By training with the loss function (14), our autoencoder attempts to accurately reconstruct the training data while satisfying linear dynamics in the latent space.

We note that higher-order terms can be included in the SINDy library (9), but as demonstrated in Appendix B, such terms can cause instabilities during prediction without improving accuracy. In practice, the nonlinearity of the autoencoder is often sufficient to model complex dynamics even when the latent space dynamics are restricted to be linear.

2.4. Gaussian Process Interpolation

After training, we require a method to obtain SINDy coefficients $\Xi^{(*)}$ for a new test parameter $\boldsymbol{\mu}^{(*)}$. Here, we use the Gaussian Process (GP) interpolation scheme of Gaussian Process-based LaSDI (GPLaSDI). We refer the reader to Bonneville et al. [6] for full details of the interpolation and only provide a brief description here.

For each entry of the coefficient matrix, we fit a GP to the training data to find obtain the mapping

$$\mathcal{GP}_{\Xi} : \boldsymbol{\mu}^{(*)} \mapsto \{m(\Xi^{(*)}), s(\Xi^{(*)})\}, \quad (15)$$

where m is the predictive mean of $\Xi^{(*)}$ and s the predictive standard deviation. When predicting for a test parameter $\boldsymbol{\mu}^{(*)}$, we have two choices evolving the compressed initial condition. Our first choice is to evolve in the latent space using the mean SINDy coefficients provided by the GPs. However, we can also sample the GPs for each SINDy coefficient several times to get multiple predictions for latent space dynamics. Decoding these predictions provides a different reconstructions of the state vector for each sample. Calculating the variance of these predictions, we obtain a measure of uncertainty for GPLaSDI without any knowledge of the governing equations.

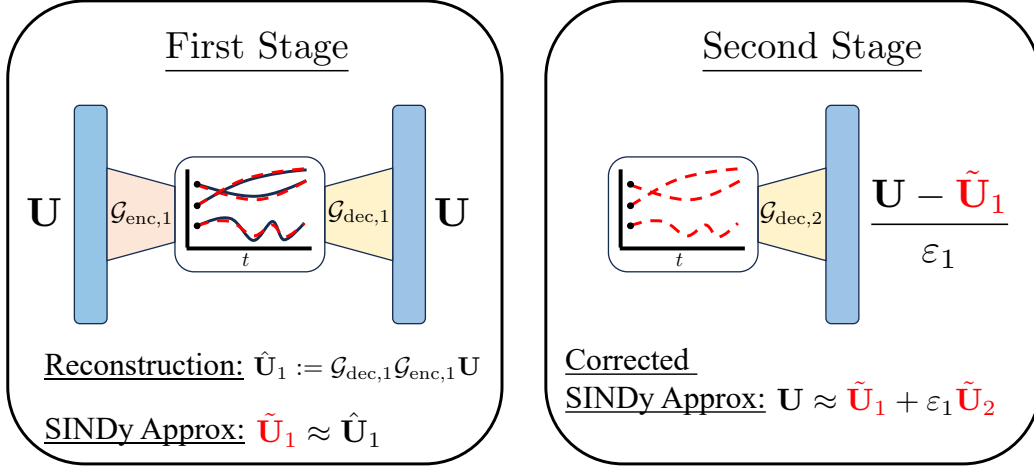


Figure 1: Schematic of mLaSDI. The first stage learns an autoencoder which is trained to reconstruct the data while learning SINDy dynamics in the latent space. The latent trajectories (solid black lines) are approximated using SINDy (dashed red lines). In the second stage, a new decoder maps the SINDy-approximated latent trajectories to the normalized residual from the first stage. The final reconstruction combines outputs from both decoders.

3. mLaSDI

Training with the loss function (14) requires the autoencoder to simultaneously reconstruct the training data and produce latent trajectories satisfying linear ODEs. These two objectives heavily restricts the representations the autoencoder can learn compared to networks trained without dynamics constraints. As we demonstrate in Section 4, placing these restrictions on the autoencoder may inhibit us from learning accurate representations of the training data, particularly for complex or high-frequency dynamics.

Multi-stage Latent Space Dynamics Identification (mLaSDI) addresses this limitation by training additional decoders that correct the residual error from earlier stages. Using multiple stages, we are able to improve prediction errors and reduce training time compared to using a single autoencoder. This also allows us to perform less hyperparameter searching, as we are able to implement multiple smaller models to achieve high accuracy. Figure 1 provides a diagram detailing the mLaSDI framework.

3.1. Multi-stage training

The first stage of mLaSDI is identical to the GPLaSDI algorithm as described in Section 2. For training data \mathbf{U} , we obtain an autoencoder reconstruction of training data from the first stage $\hat{\mathbf{U}}_1$. We can also obtain SINDy reconstructions of the training data by decoding our SINDy approximations of the latent space dynamics, i.e.

$$\tilde{\mathbf{U}}_1 := \mathcal{G}_{\text{dec},1}(\hat{\mathbf{Z}}), \quad (16)$$

where the subscript refers to the fact that this is our first stage of training and $\hat{\mathbf{Z}}$ is our SINDy approximation of the latent trajectories \mathbf{Z} .

After training the first stage, it may be the case that the training data is not reconstructed accurately by the SINDy approximation $\tilde{\mathbf{U}}_1$. When this happens, we have no hope of accurately predicting solutions for unseen input parameters. So, with the goal of improving our SINDy reconstruction accuracy, we consider the residual between the true training data \mathbf{U} and the SINDy reconstructions of the training data $\tilde{\mathbf{U}}_1$,

$$\mathbf{R}_1 = \mathbf{U} - \tilde{\mathbf{U}}_1. \quad (17)$$

In mLaSDI, we introduce a second decoder which takes the first stage SINDy latent space trajectories as input, and attempts to reconstruct the (normalized) residual (17). More precisely, we fix model parameters of the first autoencoder, and learn a mapping for the second stage $\mathcal{G}_{\text{dec},2} : \mathbb{R}^{N_z} \rightarrow \mathbb{R}^{N_u}$ by minimizing

$$\mathcal{L}_{\text{dec},2}(\boldsymbol{\theta}_{\text{dec},2}) = \|\varepsilon_1^{-1} \mathbf{R}_1 - \mathcal{G}_{\text{dec},2} \hat{\mathbf{Z}}\|^2, \quad \varepsilon_1 = \text{std}(\mathbf{R}_1). \quad (18)$$

Here, ε_1 is a scalar which normalizes the residual to have unit standard deviation. With this approach we can sequentially train multiple models so that at stage k , we train a decoder to approximate the normalized residual from stage $k-1$. The full mLaSDI approximation is then

$$\mathbf{U} \approx \tilde{\mathbf{U}}_1 + \varepsilon_1 \tilde{\mathbf{U}}_2 + \varepsilon_2 \tilde{\mathbf{U}}_3 + \dots + \varepsilon_{n-1} \tilde{\mathbf{U}}_n, \quad (19)$$

where $\tilde{\mathbf{U}}_k$ is the decoded SINDy trajectory from the k^{th} stage $\tilde{\mathbf{U}}_k = \mathcal{G}_{\text{dec},k} \hat{\mathbf{Z}}$, and $\varepsilon_k = \text{std}(\mathbf{R}_k)$ normalizes standard deviation of the k^{th} residual to 1. Crucially, all stages share the same latent trajectories $\hat{\mathbf{Z}}$, preserving the interpretability of the learned dynamics.

We will show in Section 4 that introducing one stage of training is enough to achieve significant increase in reconstruction and prediction accuracy.

3.2. Architecture of the later stages

After the first stage of training, we are free to choose any architecture for the decoders at later stages. Our goal is to require minimal hyperparameter tuning, and so we adopt the approach of Wang and Lai [52]. All stages have identical decoder architectures, varying only the activation functions. For all training stages after the first, we use sine activation on the first layer. Sinusoidal activations enable neural networks to represent high-frequency content more effectively [47, 52], which is important because the residuals often contain fine-scale features that the dynamics-constrained first stage cannot capture. Subsequent layers use the hyperbolic tangent activation.

A key element of the multistage networks in Wang and Lai [52] is the introduction of a scaling factor κ that is used to initialize weights at later layers. Their work focuses mostly on multi-layer perceptrons and PINNs, where the networks learn an explicit coordinate-to-output mapping. In their case, the scaling factor is chosen based on the frequency of the residual, and this factor helps to accelerate learning when the residual is small.

In LaSDI we are concerned with autoencoders that learn explicit data-to-data mappings, and so the same theory does not directly transfer. Additionally, because we are compressing the data and learning latent dynamics, achieving the machine-precision accuracy sought after in the original work is not feasible. Empirically, we find that $\kappa = 1$ provides the best balance between accuracy and training efficiency. Based on the numerical study in Appendix A, we set $\kappa = 1$ in all the numerical results below.

4. Numerical examples

Here, we provide three numerical examples to demonstrate the performance of mLaSDI compared to GPLaSDI. We will show that mLaSDI allows us to train more accurate models in less time, and is less sensitive to choice of model architecture. Moreover, mLaSDI often outperforms larger GPLaSDI models and achieves greater parameter efficiency. Although we focus on GPLaSDI, the mLaSDI framework applies to any LaSDI variant, and we expect similar improvements for other formulations.

All first-stage autoencoders use Softplus activation function and are trained for a fixed number of iterations using Pytorch’s implementation of the ADAM optimizer [36]. When optimizing the GP parameters for our SINDy coefficients, we use the `GaussianProcessRegressor` from scikit-learn [42]. We use the

Table 1: Results applying GPLaSDI and mLaSDI for toy problem (21) and wake shedding (23). mLaSDI used two training stages and the reported number of training epochs are for both stages combined.

Problem	Model	Architecture	Training Epochs	Relative Error
Toy Problem	GPLaSDI	600-200-20-10	50,000	4–20%
Toy Problem	GPLaSDI	600-200-100-50-20-10	50,000	3–25%
Toy Problem	mLaSDI	600-200-20-10	20,000	0.1–3%
Wake Shedding	GPLaSDI	2934-50-5	10,000	3–5%
Wake Shedding	GPLaSDI	2934-100-50-25-5	10,000	2–4%
Wake Shedding	mLaSDI	2934-50-5	5,000	1–2%

Matérn kernel

$$k(\mathbf{x}, \mathbf{y}) = \frac{1}{\Gamma(\nu)2^{\nu-1}} \left(\frac{\sqrt{2\nu}}{l} \|\mathbf{x} - \mathbf{y}\| \right)^\nu K_\nu \left(\frac{\sqrt{2\nu}}{l} \|\mathbf{x} - \mathbf{y}\|^2 \right), \quad (20)$$

where $\Gamma(\cdot)$ is the Gamma function, K_ν is a modified Bessel function, and we set $\nu = 1.5$. We set the hyperparameters of the loss function (14) to $\beta_1 = 10^{-1}$, $\beta_2 = 10^{-3}$.

We describe network architectures using the notation $N_{\text{in}}-h_1-h_2-\dots-N_z$, where N_{in} is the input dimension, h_i are hidden layer widths, and N_z is the latent dimension. For example the notation 1000-100-10-5, which represents a fully connected network with input dimension 1000, two hidden layers (sizes 100 and 10), and output dimension 5. The decoder always has the reverse architecture of the encoder, e.g. 5-10-100-1000. In each example, we obtain training data reconstructions and test data predictions for input parameters by evolving latent dynamics using ODEs which correspond to the mean SINDy coefficients from our GPs.

4.1. Multiscale oscillating system

We begin with a simple example to illustrate the spectral bias limitation of standard LaSDI. Consider the multiscale function

$$f(x, t; A) = A [\sin(2x - t) + 0.1 \cos((40x + 2t) \sin(t))] e^{-x^2}, \quad (21)$$

where the input parameter A controls the amplitude of the function. This function combines a low-frequency sine wave with a small, high-frequency

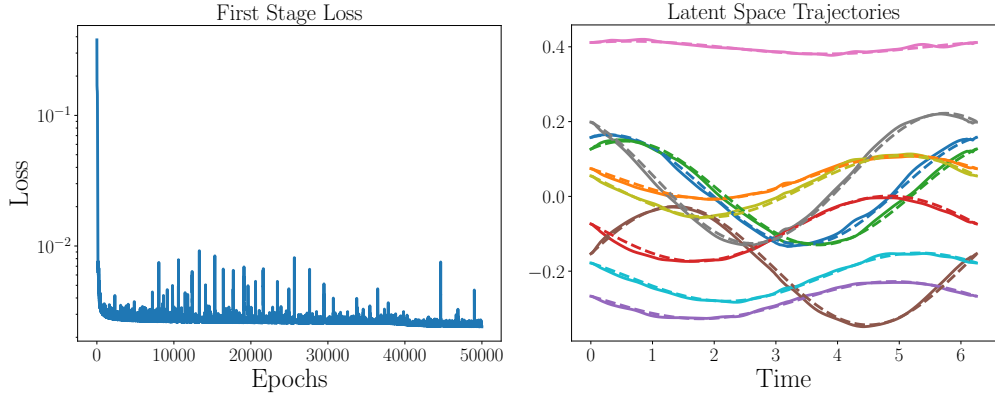


Figure 2: Applying GPLaSDI to toy problem (21). (Left) Loss for GPLaSDI and (Right) Latent space trajectories of autoencoder (solid lines) and SINDy approximation (dashed lines) for training case $A = 1.4$.

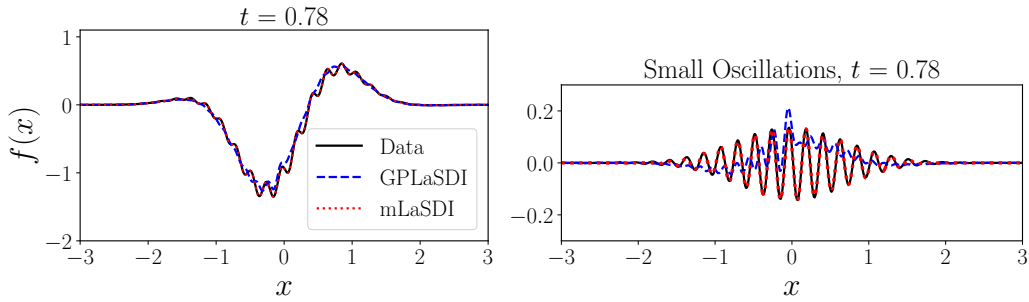


Figure 3: Applying GPLaSDI and mLaSDI with 2 stages to (21) with $A = 1.4$. (Left) Reconstruction of the training data for both methods. (Right) Results after subtracting the sine wave from the approximations to visualize how well each method approximates the small, high-frequency cosine wave. Note that the data and mLaSDI are nearly overlapping.

cosine component to emphasize the setting where dynamics-constrained autoencoders struggle due to spectral bias.

We generate synthetic training data from the input parameter values $A \in \{1.0, 1.4\}$, and try to predict for the case $A = 1.2$. To generate data for this toy problem, we sample (21) at 201 time steps evenly distributed on the interval $[0, 2\pi]$, and 600 spatial steps evenly distributed in the interval $[-3, 3]$. This yields 201 snapshots of the state vectors $\mathbf{u}(t; A) \in \mathbb{R}^{600}$.

We train two stages of mLaSDI for 10,000 iterations each. For comparison, we also train one stage of GPLaSDI for 50,000 iterations to emphasize that one stage of training is insufficient to accurately capture dynamics of the data. Our autoencoders for both mLaSDI and GPLaSDI have the same architecture, consisting of 2 hidden layers with architecture 600-200-20-10. We then train our models for this toy problem on CPU using a 2021 MacBook Pro with Apple M1 Max Chip and 32 GB of memory.

In Figure 2 we plot the loss curve for GPLaSDI along with latent space trajectories for the training case $A = 1.4$. It is clear that training loss quickly stagnates, and the GPLaSDI model is no longer improving despite additional training. Figure 3 compares reconstructions from both methods. From this snapshot it is clear that both GPLaSDI and mLaSDI capture the behavior of the low-frequency sine wave (left panel). However, the right panel shows that, after removing the low-frequency sine component, GPLaSDI fails to accurately capture the high-frequency cosine component. This failure is not due to lack of training, but a fundamental limitation of our autoencoder with smooth latent dynamics. In contrast, mLaSDI provides a significant improvement over GPLaSDI and accurately approximates both the large sine wave and small cosine wave. The second-stage decoder quickly learns the high-frequency residual that the dynamics-constrained first stage struggles to represent.

As we see in Figure 4, GPLaSDI’s failure to capture the full behavior of the function (21) leads to training and predictive relative errors of approximately 4–20%. mLaSDI reduces this error by an order of magnitude, achieving relative errors between 0.1–3%. This simple example shows how mLaSDI significantly improves the representation power of our models over base GPLaSDI.

We also note that GPLaSDI fails to accurately reconstruct the training data even for wider and deeper autoencoders than the one used here. In Table 1 we report the results from training GPLaSDI with a larger autoencoder architecture of 600-200-100-50-20-10, which achieves relative errors on the scale of 3-25%. Despite the fact that this autoencoder has nearly $2 \times$ the

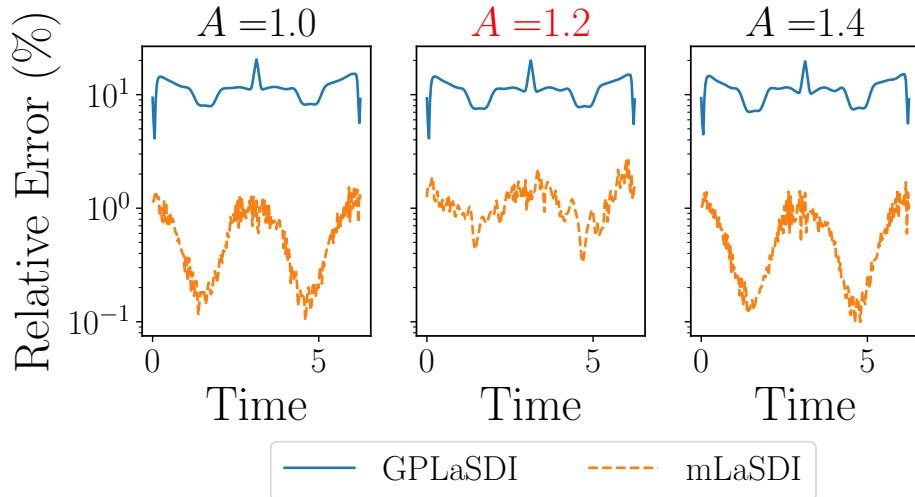


Figure 4: Relative error for GPLaSDI and mLaSDI applied to toy problem (21). GPLaSDI is trained for 50,000 iterations while mLaSDI has 2 stages each trained for 10,000 iterations. Both methods are trained on the data from cases $A = (1.0, 1.4)$, and we predict for $A = 1.2$.

number of learnable parameters as our original autoencoder, the relative error does not improve significantly, and is even worse than the smaller model for the prediction case. This emphasizes how the training approach of mLaSDI is able to outperform larger GPLaSDI models.

4.2. Unsteady Wake Flow

Next we consider unsteady wake flow, governed by the incompressible Navier–Stokes equations

$$\frac{\partial \mathbf{u}}{\partial t} + (\mathbf{u} \cdot \nabla) \mathbf{u} = -\nabla p + \nu \nabla^2 \mathbf{u} \quad \text{in } \Omega \quad (22)$$

$$\nabla \cdot \mathbf{u} = 0 \quad \text{in } \Omega, \quad (23)$$

where $\mathbf{u}(x, y, t) = (u_1(x, y, t), u_2(x, y, t))$ is the fluid velocity, p is the pressure, ν is the kinematic viscosity, and Ω is the spatial domain. The domain is a 2D rectangular $(x, y) \in [0, 1] \times [0, 2]$, with a cylinder of radius 0.05 centered at $(x, y) = (0.5, 0.5)$. We impose Dirichlet boundary condition at the inlet $\mathbf{u}(x, 0, t) = (0, 1)$. We apply homogeneous Dirichlet boundary conditions on the cylinder, and natural boundary conditions on the remaining boundaries.

In Figure 5 we display our mesh, which was generated using GMSH [22] and has 2,934 spatial nodes. We solve the incompressible Navier–Stokes equations

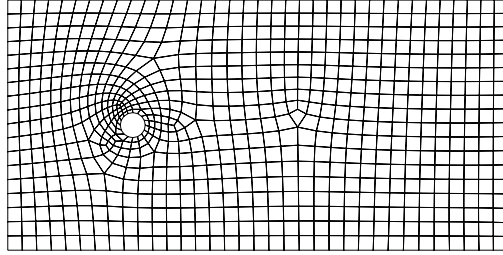


Figure 5: Mesh used to solve unsteady wake flow, rotated 90 degrees clockwise.

equations using PyMFEM’s Navier solver [2] with first-order elements and timestep $\Delta t = 0.001$ on a once-refined mesh (11,492 nodes), then downsample the solution back to the original mesh. Each simulation is run for 10 time units to establish vortex shedding, followed by 1 additional time unit from which we extract 101 snapshots (every 10th timestep). This yields state vectors $\mathbf{u}(t; \nu) \in \mathbb{R}^{2934}$ for $\nu = (0.00032, 0.00043, 0.00054)$. We train mLaSDI and GPLaSDI on the velocity magnitude of snapshots generated for $\nu = (0.00032, 0.00054)$ and predict for $\nu = 0.00043$

Autoencoders for unsteady wake flow were trained on CPU using a 2021 MacBook Pro with Apple M1 Max Chip and 32 GB of memory. Table 1 contains architectures for the training of GPLaSDI and mLaSDI. We train on the velocity magnitude data for $\nu = (0.00032, 0.00054)$, and try to predict evolution of velocity magnitude for $\nu = 0.00043$. Similar to the previous example, we train two stages of mLaSDI for 2,500 iterations each. For comparison, we also train one stage of GPLaSDI for 10,000 iterations. Our autoencoders for both methods have the same architecture, consisting of 1 hidden layer with architecture 2934-50-5.

Figure 6 shows relative errors of GPLaSDI and mLaSDI for our three kinematic viscosities. In this case, both methods produce reasonable relative errors within 5%, with mLaSDI reducing errors by only 1–3% compared to GPLaSDI. While this improvement is more modest than the order-of-magnitude gains observed for the multiscale problem, the qualitative differences are still notable. In Figure 7 we plot a snapshot of the solutions to demonstrate that there is still a visible qualitative difference between GPLaSDI and mLaSDI. The vortices of the GPLaSDI prediction are more circular than the true vortices, and additionally the background velocity field has some visible noise in the error. In contrast, mLaSDI produces more elongated vortices which are closer in shape to the true data, while also produces a smoother background velocity

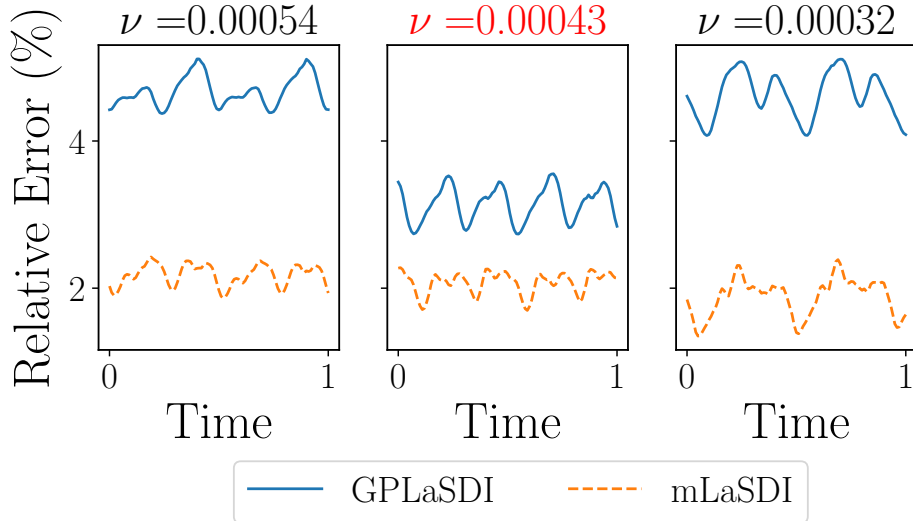


Figure 6: Relative error for GPLaSDI and mLaSDI applied to unsteady wake flow. GPLaSDI is trained for 10,000 iterations while mLaSDI has 2 stages each trained for 2,500 iterations. Both methods are trained on the data from cases $\nu = (0.00032, 0.00054)$, and we predict for $\nu = 0.00043$.

field. So, mLaSDI still provides a significant qualitative improvement over GPLaSDI for this problem even though the quantitative decrease in relative error is only 1–3 percentage points.

Table 1 also reports results for a larger GPLaSDI architecture (2934-100-50-25-5), which has more than twice the parameters of the baseline. The larger GPLaSDI model achieves relative errors of approximately 2–4%, which is still less accurate than our smaller mLaSDI model which has only $1.5\times$ the number of parameters in our original first stage. This again emphasizes the greater parameter efficiency we achieve through altering the training process with mLaSDI rather than training a larger model.

4.3. Two stream plasma instability

Our previous examples demonstrated that mLaSDI achieves improved accuracy over GPLaSDI models with identical architectures. Here, we show that mLaSDI with smaller networks can outperform GPLaSDI with substantially more parameters, achieving higher accuracy in less training time.

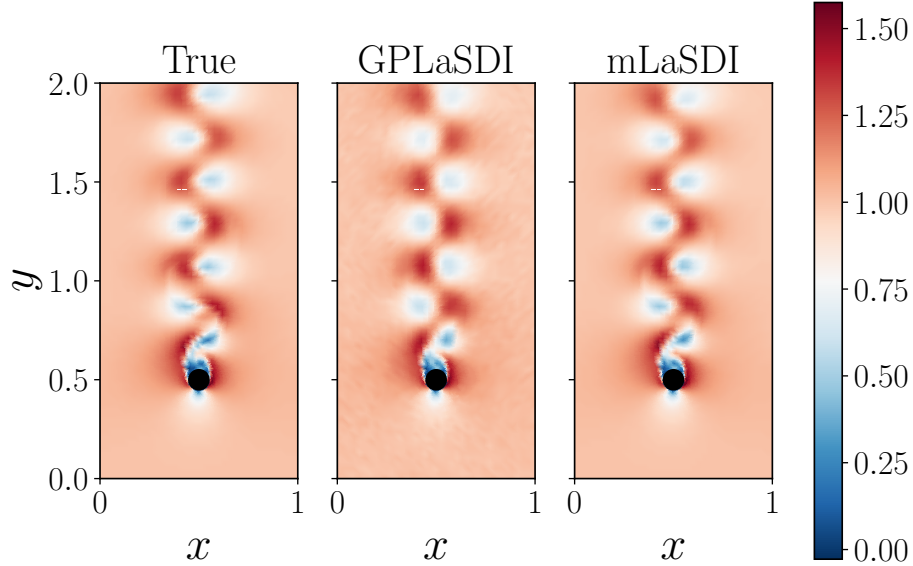


Figure 7: Snapshot of velocity magnitude for wake shedding (23) problem at $t = 0.5$ for the interpolation case $\nu = 0.00043$.

For our final example, we consider the 1D-1V Vlasov equation

$$\begin{cases} \frac{\partial f}{\partial t} + \frac{\partial v f}{\partial x} + \frac{\partial}{\partial v} \left(\frac{d\Phi}{dx} f \right) = 0, & t \in (0, 5], x \in [0, 2\pi], v \in [-7, 7] \\ \frac{d^2 \Phi}{dx^2} = \int_v f dv, \\ f(x, v, 0; \boldsymbol{\mu}) = \frac{8}{\sqrt{2\pi T}} \left[1 + 0.1 \cos(kx) \right] \left[\exp \left(-\frac{(v-2)^2}{2T} \right) + \exp \left(-\frac{(v+2)^2}{2T} \right) \right]. \end{cases} \quad (24)$$

Here, $f(x, v, t)$ is the electron distribution function which depends on space x and velocity v . The function $\Phi(x)$ is the electrostatic potential. Our initial condition consists of two streams centered at $v = \pm 2$, and is parameterized by $\boldsymbol{\mu} = (T, k)^\top$. These parameters control the width and periodicity of the two initial streams. This configuration exhibits the two-stream instability, causing the beams to merge and form vortical structures in phase space.

We solve the 1D-1V Vlasov equation using HyPar [30] with a WENO spatial discretization scheme [32] and fourth-order Runge–Kutta time integration scheme with timestep $\Delta t = 0.005$. We consider the parameter domain $(T, k) \in [0.9, 1.1] \times [1.0, 1.2]$, discretized with spacing $\Delta T = \Delta k = 0.01$ to

Table 2: Model architectures used to train GPLaSDI and mLaSDI for 1D-1V Vlasov experiments.

Component	Choices	Description
mLaSDI Hidden Layers	50, 500, 1000, 500-50, 1000-500-50	Fully connected layers
GPLaSDI Hidden Layers	75, 750, 1500, 750-75, 1500-750-75	Fully connected layers
Latent Dimension	4, 5, 6, 7	Bottleneck dimension
GPLaSDI Training Config	25k, 50k, 75k, 100k	Training checkpoints
mLaSDI Training Config.	(25k,25k), (25k,50k), (50k,50k), (75k,25k)	(Stage 1, Stage 2) iter. pairs

produce 441 parameter combinations. To generate data, we sample the solution at every timestep from a uniform 64×64 grid in the space-velocity field to obtain 251 snapshots of our state vectors $\mathbf{u}(t; \boldsymbol{\mu}) \in \mathbb{R}^{4096}$. We then take snapshots from 25 full-order model solutions on a 5×5 uniform grid as training data, and attempt to predict for the other parameters.

Training is performed on an NVIDIA V100 GPU via the LLNL Lassen cluster. We train mLaSDI using a wide range of architectures, latent space dimensions, and training iterations, with full experiment details given in Table 2. To ensure a fair comparison, GPLaSDI hidden layers are widened by a factor of 1.5 relative to mLaSDI. The second stage of mLaSDI requires training a new decoder, so a 2-stage model has approximately $1.5 \times$ the number of parameters as a single-stage model. For this experiment, the hidden layers for GPLaSDI were widened by a factor of 1.5 compared to mLaSDI, leading to GPLaSDI models which have approximately $2.25 \times$ more parameters than the first stage of mLaSDI and $1.5 \times$ the parameters as our 2-stage mLaSDI models. Our goal here is to demonstrate that the multi-stage training achieves superior performance with fewer model parameters.

To evaluate our results, we define the relative error between a full-order simulation $\mathbf{u}(t; \boldsymbol{\mu}^{(*)})$ and the mLaSDI approximation $\tilde{\mathbf{u}}(t; \boldsymbol{\mu}^{(*)})$ as

$$r^{(*)} := \max_{j=0, \dots, N_t} \frac{\|\mathbf{u}(t_j; \boldsymbol{\mu}^{(*)}) - \tilde{\mathbf{u}}(t_j; \boldsymbol{\mu}^{(*)})\|}{\|\mathbf{u}(t_j; \boldsymbol{\mu}^{(*)})\|}, \quad (25)$$

where $\|\cdot\|$ is the usual Euclidean norm.

Figure 8 shows the error distribution across the parameter space for a representative mLaSDI model with architecture 4096-500-5. After the first stage, errors range from approximately 7–9% throughout the domain. The second stage reduces errors substantially, achieving below 2% for most parameters and below 1% near the training points.

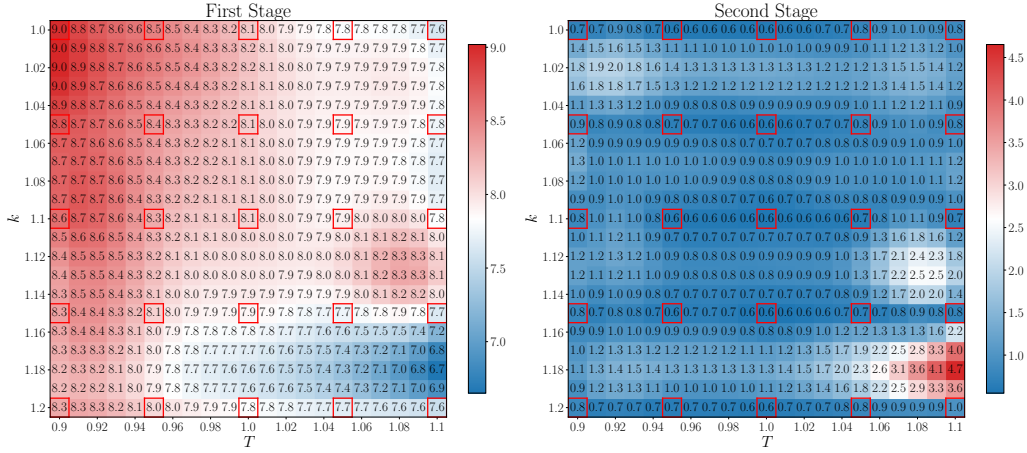


Figure 8: Maximum relative errors when applying mLaSDI with two stages to 1D-1V Vlasov equation with architecture 4096-500-5, where each stage is trained for 25,000 iterations. Red boxes indicate training parameters and the rest are predicted. We see that the second stage of training significantly lowers the maximum relative error achieved compared to only one stage of training.

Figure 9 the errors from each model along with training time. The reported training times for the mLaSDI represent the total time to train both the first and second stages. We see that mLaSDI consistently produces lower maximum, mean, and minimum relative errors than GPLaSDI models despite using fewer model parameters. For some models, introduction of a second stage also allows us to achieve maximum relative errors below 1% for some architectures, which we never achieve by training only one stage of GPLaSDI. Aggregating across all configurations, mLaSDI reduces the median error by factors of 2.54, 3.24, and 5.91 for the maximum, mean, and minimum errors, respectively compared to GPLaSDI models trained for the same number of iterations. We also see that mLaSDI has much greater variance between the maximum and minimum relative errors compared to GPLaSDI. This is expected, as the second stage in mLaSDI minimizes the reconstruction error on training data and so reconstruction error at these points will be much lower than GPLaSDI or the first stage.

5. Discussion

We have introduced multi-stage Latent Space Dynamics Identification (mLaSDI), a framework that extends LaSDI variants by sequentially train-

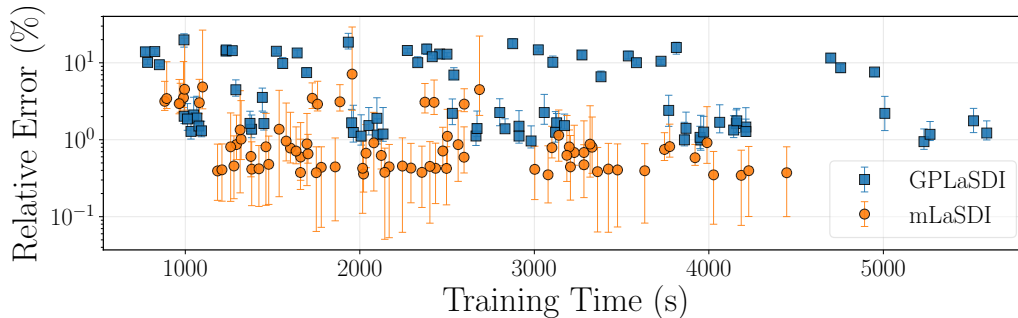


Figure 9: Applying mLaSDI and GPLaSDI to 1D-1V Vlasov equation using a wide range of architectures in Table 2. Error bars indicate the maximum and minimum relative errors throughout the parameter space, and markers indicate the median relative error (using the error metric (25)).

ing additional decoders to correct residual errors from earlier stages. By decoupling reconstruction accuracy from the dynamics-constrained first stage, mLaSDI overcomes the fundamental tension between interpretable latent dynamics and representational capacity that limits standard LaSDI approaches. Numerical experiments on a multiscale oscillating system, unsteady wake flow past a cylinder, and the 1D-1V Vlasov equation demonstrate that mLaSDI achieves consistently higher training a prediction accuracy over GPLaSDI. These improvements stem from the multi-stage architecture rather than increased model capacity, and the second-stage decoder efficiently captures high-frequency residuals that the dynamics-constrained first stage cannot represent.

Our results suggest that LaSDI variants face a fundamental tension between interpretability of dynamics in the latent space and representational capacity. Smooth latent dynamics are desirable for interpretability and stability of our models, but limit accurate reconstruction of high-frequency data. Multi-stage training offers a resolution to this problem. The first stage captures interpretable, low-frequency dynamics, while subsequent stages recover fine-scale features without sacrificing interpretability of the latent space.

Several limitations and interesting aspects of mLaSDI must still be explored. One possible approach is integrating weak SINDy [38] rather than strong SINDy, which has been shown to improve prediction accuracy even without noisy data [25, 49]. It remains unclear how to apply mLaSDI without overfitting noisy data, and mLaSDI may overfit noise during higher stages. Here, we restricted attention to linear latent dynamics for stability reasons

(Appendix [Appendix B](#)), but richer dynamics could improve accuracy if instabilities can be controlled. Additionally, the choice of two stages was sufficient for all examples considered, but systematic guidelines for selecting the number of stages and their relative training budgets remain to be developed. These extensions offer exciting opportunities for further advancing the mLaSDI framework.

Acknowledgements

This work was partially supported by the Lawrence Livermore National Laboratory (LLNL) under Project No. 50284. Robert Stephany was supported by the Sydney Fernbach Postdoctoral Fellowship under LDRD number 25-ERD- 049. Y. Choi was also supported for this work by the U.S. Department of Energy, Office of Science, Office of Advanced Scientific Computing Research, as part of the CHaRMNET Mathematical Multifaceted Integrated Capability Center (MMICC) program, under Award Number DE-SC0023164. Livermore National Laboratory is operated by Lawrence Livermore National Security, LLC, for the U.S. Department of Energy, National Nuclear Security Administration under Contract DE-AC52-07NA27344. LLNL document release number: LLNL-JRNL-2014430.

References

- [1] Z. Aldirany, R. Cottureau, M. Laforest, and S. Prudhomme. Multi-level neural networks for accurate solutions of boundary-value problems. *Computer Methods in Applied Mechanics and Engineering*, 419:116666, 2024. ISSN 0045-7825. doi: <https://doi.org/10.1016/j.cma.2023.116666>.
- [2] R. Anderson et al. Mfem: A modular finite element methods library. *Computers & Mathematics with Applications*, 81:42–74, 2021.
- [3] P. Benner, S. Gugercin, and K. Willcox. A survey of projection-based model reduction methods for parametric dynamical systems. *SIAM Review*, 57(4):483–531, 2015. doi: 10.1137/130932715.
- [4] P. Benner, P. Goyal, B. Kramer, B. Peherstorfer, and K. Willcox. Operator inference for non-intrusive model reduction of systems with non-polynomial nonlinear terms. *Computer Methods in Applied Mechanics and Engineering*, 372:113433, 2020.

- [5] G. Berkooz, P. Holmes, and J. L. Lumley. The proper orthogonal decomposition in the analysis of turbulent flows. *Annual review of fluid mechanics*, 25(1):539–575, 1993.
- [6] C. Bonneville, Y. Choi, D. Ghosh, and J.L. Belof. Gplasi: Gaussian process-based interpretable latent space dynamics identification through deep autoencoder. *Computer Methods in Applied Mechanics and Engineering*, 418:116535, 2024. ISSN 0045-7825. doi: <https://doi.org/10.1016/j.cma.2023.116535>.
- [7] C. Bonneville et al. A comprehensive review of latent space dynamics identification algorithms for intrusive and non-intrusive reduced-order modeling. *arXiv preprint arXiv:2403.10748*, 2024.
- [8] Aaron L Brown, Eric B Chin, Youngsoo Choi, Saad A Khairallah, and Joseph T McKeown. A data-driven, non-linear, parameterized reduced order model of metal 3d printing. *arXiv preprint arXiv:2311.18036*, 2023.
- [9] S.L. Brunton, J.L. Proctor, and J.N. Kutz. Discovering governing equations from data by sparse identification of nonlinear dynamical systems. *Proceedings of the National Academy of Sciences*, 113(15):3932–3937, 2016. doi: [10.1073/pnas.1517384113](https://doi.org/10.1073/pnas.1517384113).
- [10] M. Calder, C. Craig, D. Culley, R. de Cani, C. A. Donnelly, R. Douglas, B. Edmonds, J. Gascoigne, N. Gilbert, C. Hargrove, F. Hinds, D. C. Lane, D. Mitchell, G. Pavey, D. Robertson, B. Rosewell, S. Sherwin, M. Walport, and A. Wilson. Computational modelling for decision-making: where, why, what, who and how. *Royal Society Open Science*, 5(6):172096, 2018. doi: [10.1098/rsos.172096](https://doi.org/10.1098/rsos.172096).
- [11] K. Champion, B. Lusch, J. N. Kutz, and S. L. Brunton. Data-driven discovery of coordinates and governing equations. *Proceedings of the National Academy of Sciences*, 116(45):22445–22451, 2019.
- [12] Youngsoo Choi, Gabriele Boncoraglio, Spenser Anderson, David Am-sallem, and Charbel Farhat. Gradient-based constrained optimization using a database of linear reduced-order models. *Journal of Computational Physics*, 423:109787, 2020.

- [13] Youngsoo Choi, Deshawn Coombs, and Robert Anderson. Sns: A solution-based nonlinear subspace method for time-dependent model order reduction. *SIAM Journal on Scientific Computing*, 42(2):A1116–A1146, 2020.
- [14] Youngsoo Choi, Peter Brown, William Arrighi, Robert Anderson, and Kevin Huynh. Space–time reduced order model for large-scale linear dynamical systems with application to boltzmann transport problems. *Journal of Computational Physics*, 424:109845, 2021.
- [15] Seung Whan Chung, Youngsoo Choi, Pratanu Roy, Thomas Moore, Thomas Roy, Tiras Y Lin, Du T Nguyen, Christopher Hahn, Eric B Duoss, and Sarah E Baker. Train small, model big: Scalable physics simulators via reduced order modeling and domain decomposition. *Computer Methods in Applied Mechanics and Engineering*, 427:117041, 2024.
- [16] Seung Whan Chung, Christopher Miller, Youngsoo Choi, Paul Tranquilli, H Keo Springer, and Kyle Sullivan. Latent space dynamics identification for interface tracking with application to shock-induced pore collapse. *arXiv preprint arXiv:2507.10647*, 2025.
- [17] Dylan Matthew Copeland, Siu Wun Cheung, Kevin Huynh, and Youngsoo Choi. Reduced order models for lagrangian hydrodynamics. *Computer Methods in Applied Mechanics and Engineering*, 388:114259, 2022.
- [18] M. Cranmer et al. Discovering symbolic models from deep learning with inductive biases. *Advances in Neural Information Processing Systems*, 33:17429–17442, 2020.
- [19] R. M. Cummings, W. H. Mason, S. A. Morton, and D. R. McDaniel. *Applied computational aerodynamics: A modern engineering approach*, volume 53. Cambridge University Press, 2015.
- [20] A. N. Diaz, Y. Choi, and M. Heinkenschloss. A fast and accurate domain decomposition nonlinear manifold reduced order model. *Computer Methods in Applied Mechanics and Engineering*, 425:116943, 2024.
- [21] W.D. Fries, X. He, and Y. Choi. Lasdi: Parametric latent space dynamics identification. *Computer Methods in Applied Mechanics and Engineering*, 399:115436, 2022. ISSN 0045-7825. doi: <https://doi.org/10.1016/j.cma.2022.115436>.

- [22] C. Geuzaine and J.F. Remacle. Gmsh: A 3-d finite element mesh generator with built-in pre- and post-processing facilities. *International Journal for Numerical Methods in Engineering*, 79(11):1309–1331, 2009. doi: <https://doi.org/10.1002/nme.2579>.
- [23] Xavier Glorot and Yoshua Bengio. Understanding the difficulty of training deep feedforward neural networks. In *Proceedings of the thirteenth international conference on artificial intelligence and statistics*, pages 249–256. JMLR Workshop and Conference Proceedings, 2010.
- [24] X. He, Y. Choi, W.D. Fries, J.L. Belof, and J. Chen. glasdi: Parametric physics-informed greedy latent space dynamics identification. *Journal of Computational Physics*, 489:112267, 2023. ISSN 0021-9991. doi: <https://doi.org/10.1016/j.jcp.2023.112267>.
- [25] X. He, A. Tran, D.M. Bortz, and Y. Choi. Physics-informed active learning with simultaneous weak-form latent space dynamics identification. *International Journal for Numerical Methods in Engineering*, 126(1): e7634, 2025. doi: <https://doi.org/10.1002/nme.7634>.
- [26] Xiaolong He, Youngsoo Choi, William D Fries, Jonathan L Belof, and Jiun-Shyan Chen. Certified data-driven physics-informed greedy auto-encoder simulator. *arXiv preprint arXiv:2211.13698*, 2022.
- [27] Xiaolong He, Yeonjong Shin, Anthony Gruber, Sohyeon Jung, Kookjin Lee, and Youngsoo Choi. Thermodynamically consistent latent dynamics identification for parametric systems. *arXiv preprint arXiv:2506.08475*, 2025.
- [28] G. E. Hinton and R. R. Salakhutdinov. Reducing the dimensionality of data with neural networks. *Science*, 313(5786):504–507, 2006.
- [29] A.A. Howard, S.H. Murphy, S.E. Ahmed, and P. Stinis. Stacked networks improve physics-informed training: Applications to neural networks and deep operator networks. *Foundations of Data Science*, 7(1):134–162, 2025. doi: 10.3934/fods.2024029.
- [30] HyPar. HyPar repository. <https://bitbucket.org/deboghosh/hypar>, 2025.

- [31] O. Issan and B. Kramer. Predicting solar wind streams from the inner-heliosphere to earth via shifted operator inference. *arXiv preprint arXiv:2203.13372*, 2022.
- [32] G.-S. Jiang and C.-W. Shu. Efficient implementation of weighted ENO schemes. *Journal of Computational Physics*, 126(1):202–228, 1996. doi: 10.1006/jcph.1996.0130.
- [33] D. Jones, C. Snider, A. Nassehi, J. Yon, and B. Hicks. Characterising the digital twin: A systematic literature review. *CIRP Journal of Manufacturing Science and Technology*, 29:36–52, 2020. ISSN 1755-5817. doi: <https://doi.org/10.1016/j.cirpj.2020.02.002>.
- [34] Y. Kim, Y. Choi, D. Widemann, and T. Zohdi. A fast and accurate physics-informed neural network reduced order model with shallow masked autoencoder. *Journal of Computational Physics*, 451:110841, 2022.
- [35] Youngkyu Kim, Karen Wang, and Youngsoo Choi. Efficient space–time reduced order model for linear dynamical systems in python using less than 120 lines of code. *Mathematics*, 9(14):1690, 2021.
- [36] D. P. Kingma and J. Ba. Adam: A method for stochastic optimization. *arXiv preprint arXiv:1412.6980*, 2014.
- [37] Sean McBane and Youngsoo Choi. Component-wise reduced order model lattice-type structure design. *Computer methods in applied mechanics and engineering*, 381:113813, 2021.
- [38] D.A. Messenger and D.M. Bortz. Weak sindy: Galerkin-based data-driven model selection. *Multiscale Modeling & Simulation*, 19(3):1474–1497, 2021. doi: 10.1137/20M1343166.
- [39] D. Noble. The rise of computational biology. *Nature Reviews Molecular Cell Biology*, 3(6):459–463, 2002.
- [40] J. Sur R. Park, S.W. Cheung, Y. Choi, and Yeonjong Shin. tlasdi: Thermodynamics-informed latent space dynamics identification. *Computer Methods in Applied Mechanics and Engineering*, 429:117144, 2024. ISSN 0045-7825. doi: <https://doi.org/10.1016/j.cma.2024.117144>.

- [41] A. T. Patera, G. Rozza, et al. *Reduced basis approximation and a posteriori error estimation for parametrized partial differential equations*. Arch Computat Methods, 2007.
- [42] F. Pedregosa, G. Varoquaux, A. Gramfort, V. Michel, B. Thirion, O. Grisel, M. Blondel, P. Prettenhofer, R. Weiss, V. Dubourg, J. Vanderplas, A. Passos, D. Cournapeau, M. Brucher, M. Perrot, and É. Duchesnay. Scikit-learn: Machine learning in python. *J. Mach. Learn. Res.*, 12(null):2825–2830, November 2011. ISSN 1532-4435.
- [43] E. Qian, B. Kramer, B. Peherstorfer, and K. Willcox. Lift & learn: Physics-informed machine learning for large-scale nonlinear dynamical systems. *Physica D: Nonlinear Phenomena*, 406:132401, 2020.
- [44] Nasim R., Aristide B., Devansh A., Felix D., Min L., Fred H., Yoshua B., and Aaron C. On the spectral bias of neural networks. In *Proceedings of the 36th International Conference on Machine Learning*, volume 97 of *Proceedings of Machine Learning Research*, pages 5301–5310. PMLR, 09–15 Jun 2019.
- [45] M. G. Safonov and R. Chiang. A schur method for balanced-truncation model reduction. *IEEE Transactions on Automatic Control*, 34(7):729–733, 1989.
- [46] M. Schmidt and H. Lipson. Distilling free-form natural laws from experimental data. *Science*, 324(5923):81–85, 2009.
- [47] V. Sitzmann, J. Martel, A. Bergman, D. Lindell, and G. Wetzstein. Implicit neural representations with periodic activation functions. In *arXiv*, 2020.
- [48] J. Thijssen. *Computational physics*. Cambridge university press, 2007.
- [49] A. Tran, X. He, D. A. Messenger, Y. Choi, and D. M. Bortz. Weak-form latent space dynamics identification. *Computer Methods in Applied Mechanics and Engineering*, 427:116998, Jul 2024.
- [50] D. Vasileska, S. M. Goodnick, and G. Klimeck. *Computational Electronics: semiclassical and quantum device modeling and simulation*. CRC press, 2017.

- [51] P. Vincent, H. Larochelle, I. Lajoie, Y. Bengio, and P. Manzagol. Stacked denoising autoencoders: Learning useful representations in a deep network with a local denoising criterion. *Journal of Machine Learning Research*, 11(110):3371–3408, 2010.
- [52] Y. Wang and C. Lai. Multi-stage neural networks: Function approximator of machine precision. *Journal of Computational Physics*, 504:112865, 2024. ISSN 0021-9991. doi: <https://doi.org/10.1016/j.jcp.2024.112865>.
- [53] Z. Xu, Y. Zhang, T. Luo, Y. Xiao, and Z. Ma. Frequency principle: Fourier analysis sheds light on deep neural networks. *Communications in Computational Physics*, 28(5):1746–1767, 2020.
- [54] Yang Yu, Yong Ma, Xiaoguang Mei, Fan Fan, Jun Huang, and Hao Li. Multi-stage convolutional autoencoder network for hyperspectral unmixing. *International Journal of Applied Earth Observation and Geoinformation*, 113:102981, 2022. ISSN 1569-8432. doi: <https://doi.org/10.1016/j.jag.2022.102981>.
- [55] J. Zabalza, J. Ren, J. Zheng, H. Zhao, C. Qing, Z. Yang, P. Du, and S. Marshall. Novel segmented stacked autoencoder for effective dimensionality reduction and feature extraction in hyperspectral imaging. *Neurocomputing*, 185:1–10, 2016. ISSN 0925-2312. doi: <https://doi.org/10.1016/j.neucom.2015.11.044>.

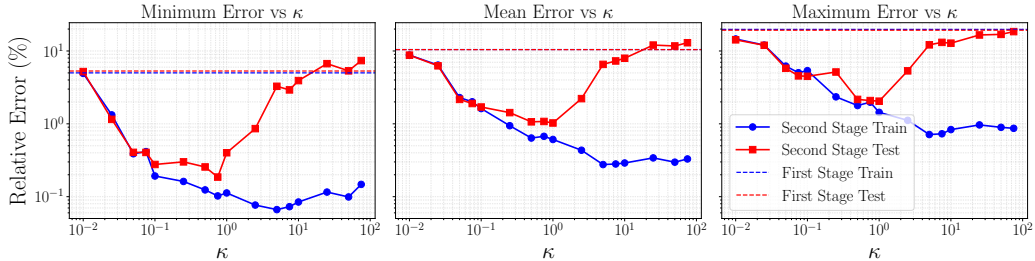


Figure A.10: Effect of scaling factor κ on mLaSDI performance for the multiscale problem (21). Each stage is trained for 10,000 epochs. Test error is minimized near $\kappa = 1$, where larger values lead to overfitting, while smaller values slow convergence.

Appendix A. Testing scaling factors

The multistage networks of Wang and Lai [52] scale weight initialization by a factor $\kappa > 0$ to accelerate residual learning in later stages. We examine how scaling the standard deviation of the weight distribution for the first layer (with sinusoidal activation) of the second-stage decoder.

We initialize scaled layers using the Xavier normal distribution [23]. For a layer mapping $\mathbb{R}^{n_{\text{in}}}$ to $\mathbb{R}^{n_{\text{out}}}$, weights are sampled from $N\left(0, G\sqrt{\frac{1}{n_{\text{in}}+n_{\text{out}}}}\right)$, where $G > 0$ is the gain. For fully connected networks, we typically use $G = 1$, though [52] suggests $G = \kappa$ for the second stage.

Since samples from $N(\mu, \sigma)$ scaled by $\eta > 0$ are distributed as $N(\eta\mu, \eta\sigma)$, using Xavier initialization with gain κ is equivalent to using gain 1 and then scaling by κ . We introduce κ into mLaSDI by defining the decoder’s first layer $L_1 : \mathbb{R}^L \rightarrow \mathbb{R}^{N_d(1)}$ as

$$L_1(z) = \sin(\kappa(W\mathbf{z} + \mathbf{b})),$$

where $L \in \mathbb{N}$ is the latent dimension and $N_d(1)$ is the first hidden layer width. We initialize $W \in \mathbb{R}^{L \times N_{\text{dec}}(1)}$ with samples from $N\left(0, \sqrt{\frac{1}{L+N_{\text{dec}}(1)}}\right)$ and set $\mathbf{b} = \mathbf{0}$. This is equivalent to sampling initial weights from $N\left(0, \kappa\sqrt{\frac{1}{L+N_{\text{dec}}(1)}}\right)$ but allows κ to be trainable.

Figure A.10 shows how κ (as a fixed parameter) impacts mLaSDI’s reconstruction and prediction accuracy across a wide range for the multiscale oscillating system of Section 4.1. Training error continues to decrease until for κ up to approximately 10. However, there is a clear minimum prediction error when setting $\kappa = 1$. For $\kappa > 1$, the model overfits the training data, and for

$\kappa < 1$ learning slows and longer training is required. Based on this empirical evidence, we choose to use $\kappa = 1$ for all of our numerical experiments.

Appendix B. Instability with second order polynomials

In this appendix, we demonstrate that higher-order polynomial terms in the SINDy library can lead to unstable predictions when interpolating for unseen parameters.

Our choice of linear latent dynamics (9) is not merely for simplicity, but also for stability. Nonlinear terms in the SINDy library can potentially introduce finite-time singularities. For instance, the simple scalar ODE $\dot{z} = z^2$ has solution $z(t) = z_0/(1 - z_0 t)$ which blows up at finite time $t = z_0^{-1}$. In contrast, linear dynamics guarantee existence for any finite time because we have

$$\dot{\mathbf{z}} = A\mathbf{z} + \mathbf{b} \implies \mathbf{z}(t) = \sum_{i=1}^n \alpha_i e^{\lambda_i t} \mathbf{w}_i - A^{-1}\mathbf{b}, \quad (\text{B.1})$$

where $(\mathbf{w}_i, \lambda_i)$ are eigenpairs of A and α_i are coefficients determined by the initial condition.

This stability guarantee is particularly critical in the LaSDI framework for two reasons. First, during training, the latent space representation evolves continuously unlike standard SINDy applications to fixed data. Nonlinear dynamics can then blow up during training as the autoencoder explores different latent representations. Second, we must interpolate SINDy coefficients for unseen parameters. Even if dynamics at training parameters $\{\boldsymbol{\mu}^{(i)}\}$ are stable, interpolation can produce coefficient combinations for $\boldsymbol{\mu}^*$ that yield unstable dynamics. Linear dynamics eliminate the risk of finite-time blowup, and provide greater stability during predictions for unseen input parameters. This stability constraint motivates our multi-stage approach, rather than pursuing accuracy through richer latent dynamics.

To demonstrate this numerically, we return to the 1D-1V Vlasov equation (24), applying only one stage of mLaSDI using the same hyperparameters as in Table 2. Training is performed on an AMD MI300A GPU via the LLNL Tuolumne cluster. Here, we expand the SINDy library to allow for pure quadratic terms (e.g., z_1^2 , z_2^2) but exclude the cross terms, such as $z_1 z_2$.

Figure B.11 compares relative errors across the parameter space when using linear and second order terms in the SINDy library. The quadratic terms slightly improve median and minimum errors for most cases. However,

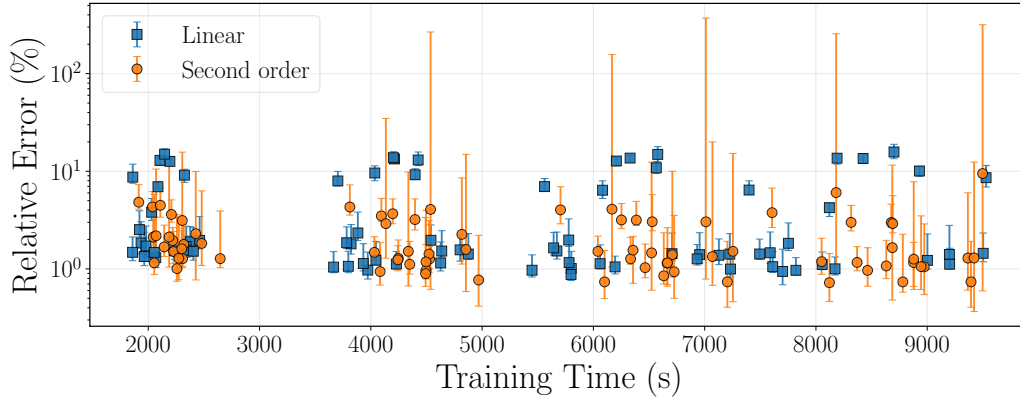


Figure B.11: Applying GPLaSDI to 1D-1V Vlasov equation using a wide range of architectures in Table 2, with linear and second order dynamics in the SINDy library. Error bars indicate the maximum and minimum relative errors throughout the parameter space, and markers indicate the median relative error.

unstable interpolations can lead to significantly larger prediction errors from the second order dynamics, resulting in relative errors over 100% for some predictions. We avoid higher-order terms in the SINDy library due to marginal accuracy gains combined with the possibility of unstable predictions at unseen parameter values.